Wideband Dual-Circular-Polarization Antenna with High Isolation for Millimeter-Wave Wireless Communications

Chao Shu, Shaoqing Hu, Xiaohe Cheng, Andre Sarker Andy, *Member, IEEE,* Yuan Yao, *Senior Member, IEEE,* Bo Zhang, *Senior Member, IEEE,* Yasir Alfadhl, *Member, IEEE,* and Xiaodong Chen, *Fellow, IEEE*

***Abstract*—This paper presents a wideband dual-circular-polarization (dual-CP) antenna with high port isolation based on a grooved-wall CP horn combined with an orthomode transducer (OMT) in the W-band. A pair of grooves on the inner wall of the horn serves as an inbuilt polarizer within the horn antenna, which is capable of generating both left-hand circular polarization (LHCP) and right-hand circular polarization (RHCP) without any septum. The continuous linearly-tapered groove design also allows this multi-section grooved-wall CP horn to achieve low reflection coefficients over a wide bandwidth, thereby realizing wideband dual-CP with high port isolation when it is used together with a wideband OMT. A prototype of the proposed dual-CP antenna is designed in simulation and measured in an experiment. The simulated and measured results agree very well, showing that port isolation $>$ 32.5 dB over 31.6% bandwidth from 80 GHz to 110 GHz is achieved with axial ratio (AR) $<$ 2.8 dB and reflection coefficient < -20 dB for both LHCP and RHCP. Rotationally symmetric radiation patterns over the entire operating bandwidth are also observed with a measured gain of 19.6$\pm$2 dBic.**

***Index Terms*—dual circular polarization, millimeter-wave (mmWave), horn antenna, wideband, isolation.**

I. Introduction

CIRCULAR-POLARIZATION (CP) antennas are preferable to Linear-Polarization (LP) antennas in various applications, such as radar [1], Global Navigation Satellite System (GNSS) [2], and satellite communications [3], [4], due to its capability of suppressing multipath fading and polarization mismatch [5]. Millimeter-Wave (mmWave) wireless communications for point-to-point (PtP) and point-to-multipoint (PtMP) high-data-rate transmission could also benefit from using CP antennas [6]. The dual-circular-polarization (dual-CP) antenna, capable of simultaneously transmitting and receiving two orthogonal CP signals [left-hand circular polarization (LHCP) and right-hand circular polarization (RHCP)], enables Polarization Division Multiplexing (PDM) [7]–[9] and In-Band Full Duplex (IBFD) [10] for mmWave wireless communication systems to achieve two-fold spectral efficiency. However, a significant level of isolation between the transmit (Tx) and receive (Rx) chains is required for the practical application of these systems, and it is anticipated that isolation $>$ 30 dB should be provided at the antenna stage [11], [12]. Therefore, a wideband dual-CP antenna with port isolation $>$ 30 dB is highly desirable in the mmWave wireless communication system offering high wireless link capacity.

A variety types of antennas and components have been proposed to realize dual CP below 60 GHz band, such as the microstrip antenna array in the microwave band below 30 GHz [13]–[18], the metasurface antenna [19], and the antenna array based on Substrate Integrated Waveguide (SIW) in the mmWave band up to 69 GHz [20]–[24]. However, the highest port isolation over the widest bandwidth reported for these types of dual-CP antenna is only isolation $>$ 20 dB over 14.7% bandwidth in the X-band [15].

Another widely used type of dual-CP antenna is based on the waveguide septum polarizer [25]. A horn antenna or a waveguide array is usually connected to the septum polarizer to achieve good dual-CP radiation performance. This structure can be applied both in the microwave band [26]–[31] and mmWave band [32], [33]. The highest port isolation over the widest bandwidth ever reported for this type of structure is port isolation $>$ 30 dB over 10% bandwidth [33]. However, it is believed that the maximum practical operating bandwidth for the septum polarizer is less than 25% [25]. Therefore, further improvement for this type of dual-CP antenna to achieve high isolation at the level of 30 dB over a bandwidth wider than 10% is quite challenging since there is also a trade-off between impedance bandwidth and axial ratio (AR) bandwidth of the septum polarizer. In [34], a novel septum polarizer using a waveguide common port with triangular cross-section is proposed to cover a bandwidth of 37.8% in the W-band and K-band, which breaks the bandwidth limit of the conventional septum polarizer with a square- or circular-waveguide common port. Nevertheless, the port isolation is only $>$ 17 dB over the operating bandwidth. Moreover, the septum inside the waveguide will pose a challenge in fabrication at high frequencies because the septum thickness will decrease as frequency increases, which limits the application of septum polarizer in the high-frequency band. Therefore, a new type of antenna structure is needed to achieve high isolation $>$ 30 dB over a wide bandwidth in the mmWave band. The iris polarizer

Manuscript received January 14, 2021; revised August 1, 2021; accepted September 6, 2021. This work was supported in part by the China Scholarship Council, National Natural Science Foundation of China under Grant No. 62001039, Grant No. 61474112, Grant 62022022 and Grant 91738102.

Chao Shu, Shaoqing Hu, Andre Sarker Andy, Yasir Alfadhl and Xiaodong Chen are with School of Electronic Engineering and Computer Science, Queen Mary University of London, London E1 4NS, UK (e-mail: xiaodong.chen@qmul.ac.uk).

Xiaohe Cheng and Yuan Yao are with School of Electronic Engineering, Beijing University of Posts and Telecommunications, Beijing, 100876, China.

Bo Zhang is with School of Electronic Science and Engineering, University of Electronic Science and Technology of China, Chengdu 610054, China.

is another type of waveguide polarizer that provides wider bandwidth when compared with the septum polarizer [35]. In [36], an iris polarizer capable of generating CP with high purity over 30% bandwidth from 5.7 - 7.7 GHz is reported, which is a good candidate to realize a wideband dual-CP antenna. However, it has to be connected to both a horn antenna and an Orthomode Transducer (OMT) to realize a dual-CP antenna, whose structure is more complicated than a dual-CP antenna based on a septum polarizer. Additionally, the thin metallic fins or periodic corrugation on the waveguide walls in the iris polarizer pose a great challenge to the fabrication in the mmWave/THz bands.

In 2019, we reported a CP antenna without any septum or extra polarizer in the W-band by introducing a pair of continuous grooves on the wall through the entire conical horn, which achieves a bandwidth of 37% [37], [38]. This structure is also capable of generating dual-CP with an orthomode transducer (OMT) and has the potential to achieve high isolation over a wide bandwidth because its continuous-tapered structure can lead to a low reflection coefficient. It is worth mentioning that another research group reported a polarizer with a grooved structure in August of 2020 [39]. This polarizer applies a single short groove on the wall of the circular waveguide to achieve dual-CP and is connected to a conical horn for radiating in the V-band. This dual-CP antenna shows a simple and compact structure with two side-fed ports as well as a mono-groove with an annulus sector cross-section being easy for fabrication. Nevertheless, the overall impedance bandwidth for both ports is relatively narrow, from 53.71 to 58.1 GHz (6.6%), and the simulated port isolation is only 15 dB within the operating bandwidth. Additionally, in [40], we have conducted a comprehensive study on the different types of waveguide-based dual-CP antennas as mentioned above.

In this paper, a multi-section horn antenna with a pair of grooves on the wall is proposed to generate dual CP with high port isolation when it is used with an orthomode transducer (OMT). Based on our previous work presented in [37], [38], we have generalized this approach and designed a multi-section grooved-wall CP horn by introducing grooves with various widths and depths in each section. An OMT based on [41] is also designed with critical modifications to significantly improve the misalignment tolerance for port isolation and polarization isolation during assembling. The operating principle of the proposed dual-CP antenna has been analyzed, and a prototype has been fabricated to verify the design in the W-band. The measured results show port isolation $>$ 30 dB and AR $<$ 2.8 dB over a bandwidth of 31.6% from 80 to 110 GHz is achieved, while the reflection coefficient is lower than -16 dB. To the best of the authors' knowledge, this is the dual-CP antenna with the highest isolation over the widest bandwidth ever reported. Furthermore, with a septum-free structure, this type of dual-CP antenna has the potential to be scaled up to even THz band. Rotationally symmetric radiation patterns over the entire operating bandwidth are also achieved with a measured gain of 19.6$\pm$2 dBic.

The remainder of this paper is organized as follows. In Section II, an overview of the entire antenna structure is described, the dual-CP generation principles of the proposed antenna is illustrated, and a parametric analysis is performed. Section III and Section IV presents the design of the multi-section grooved-wall CP horn and the OMT. In Section V, simulated and measured results are presented and discussed, followed by conclusions in Section VI.

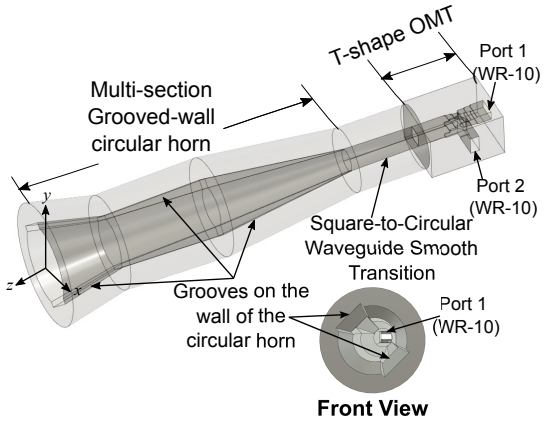

Fig. 1. Structure of the complete dual-CP antenna.

II. Antenna Structure and Operating Principle

A. Antenna Structure

The structure of the entire dual-CP antenna is presented in Fig. 1, comprising of two components. A multi-section horn with an integrated circular-to-square waveguide transformer is connected to the common port of an OMT. The horn consists of three conical sections, and a pair of grooves is introduced on the wall of each section. The grooves are aligned at 45° with respect to the x-axis, and the width and depth of the grooves in each section changes linearly. The axial port (port 1) and the lateral port (port 2) are both standard WR-10 rectangular waveguide ports. If port 1 is excited, TE_{10} mode will propagate through the OMT and be fed into the multi-section grooved-wall horn, where LHCP will be generated at the aperture of the horn; when port 2 is excited, TE_{01} mode will be guided through the OMT and fed into the multi-section grooved-wall horn, where RHCP will be generated.

B. Principle of Dual-CP Generation

Since the proposed multi-section grooved-wall horn antenna shown in Fig. 1 can be considered as a concatenation of many discretized grooved-wall circular waveguides with different dimensions, the grooved-wall circular waveguide with a uniform cross-section is used to analyze the operating principle. Firstly, the mode analysis is carried out for the cross-section of the grooved-wall circular waveguide using CST Microwave Studio (MWS). The cross-section geometry of the grooved-wall waveguide is shown in the inset of Fig. 2, where the radius of the circular waveguide (r) is 1.531 mm, depth (d) and width (w) of the grooves are 0.612 mm and 1.119 mm respectively. The mode analysis shows that two orthogonal propagating modes exist in the grooved-wall circular waveguide. The propagation constants and E-field profiles of these two modes are shown in Fig. 2.

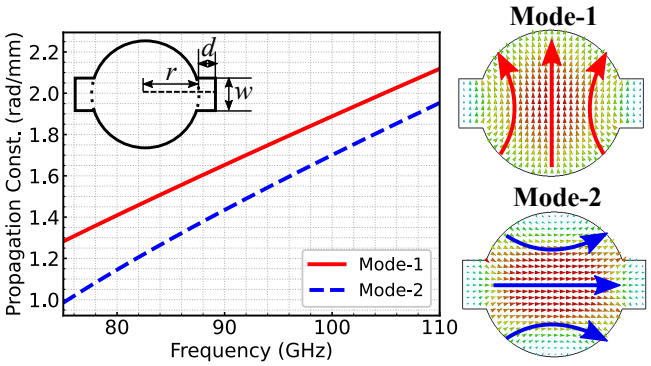

Fig. 2. Mode analysis of the grooved-wall circular waveguide.

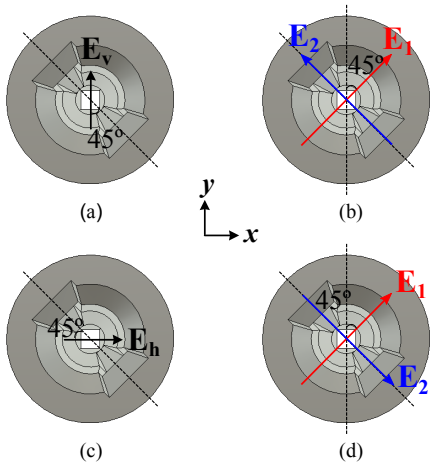

Fig. 3. Input (a) v-mode and (c) h-mode and two orthogonal degenerated modes for (b)v-mode and (d) h-mode in the grooved-wall CP horn.

When port 1 or port 2 in Fig. 1 is excited, TE_{10} (v-mode) or TE_{01} (h-mode) will be guided through the OMT to the square aperture of the square-to-circular waveguide transformer. Both modes will be converted to TE_{11} modes when they arrive at the circular waveguide section of the grooved-wall horn, and the direction of the E-field of both TE_{11} modes will be oriented at 45° with respect to the pair of grooves. Based on the mode analysis, the input TE_{11} mode will then be divided into two orthogonal degenerate TE_{11} modes, i.e., mode-1 and mode-2 in Fig. 2, due to the existence of the grooves, as shown in Fig. 3. Since it can be observed from Fig. 2 that the propagation constants of these two degenerate TE_{11} modes are different, a phase difference of $\pm 90^\circ$ between them can be achieved after propagating over a certain distance, thereby generating CP waves [38].

In order to illustrate the principle of dual-CP generation, the decomposition of v-mode and h-mode at the cross-section of grooved-wall circular waveguide is shown in Fig. 4(a) and Fig. 4(b) respectively, with the coordinates aligned with the direction of the two orthogonal degenerated modes. It can also be regarded as the front view of the grooved-wall horn aperture, and the input square waveguide port is added in the figure as a reference of the directions of E_v and E_h with respect to the input port of the groove-wall horn.

The E-field of the v-mode (E_v) can be decomposed into

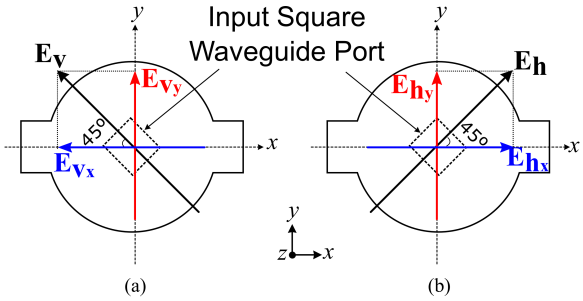

Fig. 4. The decomposition of (a) v-mode and (b) h-mode at the cross-section of grooved-wall circular waveguide.

two orthogonal components along $-x$-axis and y-axis owing to the existence of the grooves, as shown in Fig. 4(a). Let $\phi^0_{v_x}$ and $\phi^0_{v_y}$ denote the initial phases of these two orthogonal components at the start of the grooved-wall circular waveguide respectively, $\beta_{m1}(f)$ and $\beta_{m2}(f)$ denote the propagation constants of the two degenerated modes (mode-1 and mode-2 shown in Fig. 2) at frequency f respectively. The phase difference between E-fields of the two orthogonal components at frequency f after propagating over a length of l in the grooved-wall circular waveguide when the v-mode is used as the input can be written as

$$\begin{aligned}\Delta\phi_v(f) &= (\phi^0_{v_y} - \beta_{m1}(f)l) - (\phi^0_{v_x} - \beta_{m2}(f)l) \\ &= (\phi^0_{v_y} - \phi^0_{v_x}) - (\beta_{m1}(f) - \beta_{m2}(f))l \\ &= (\phi^0_{v_y} - \phi^0_{v_x}) - \Delta\beta(f)l,\end{aligned} \tag{1}$$

where $\Delta\beta(f) = \beta(f)_{m1} - \beta(f)_{m2} > 0$ is the propagation constant difference between mode-1 and mode-2 at frequency f. With given grooved-wall circular waveguide dimensions (r, d and w), $\Delta\beta(f)$ at a frequency can be obtained by mode analysis, and with a proper waveguide length l, $\Delta\beta(f)l = \pi/2$ can be achieved. Because $\phi^0_{v_y} - \phi^0_{v_x} = \pi$ according to the coordinate system (see Fig. 4(a)), it can be derived that

$$\begin{aligned}\Delta\phi_v(f) &= (\phi^0_{v_y} - \phi^0_{v_x}) - \Delta\beta(f)l \\ &= \pi - \pi/2 \\ &= \pi/2.\end{aligned} \tag{2}$$

This means with a properly designed dimension of the grooved-wall circular waveguide that leads to $\Delta\beta(f)l = \pi/2$, the phase difference between the two orthogonal degenerated modes at the end of the grooved-wall circular waveguide will be $\pi/2$. According to the analysis in our previous work, their E-field magnitudes are close to each other [38]. Therefore, an LHCP wave is generated at the end of the grooved-wall circular waveguide when the grooved-wall circular waveguide is excited with the v-mode (see Fig. 3).

Similar derivation process can be obtained when the grooved-wall circular waveguide is excited with the h-mode (see Fig. 3), but with $\phi^0_{h_y} - \phi^0_{h_x} = 0$ according to the coordinate system, as shown in Fig. 4(b), it can be derived

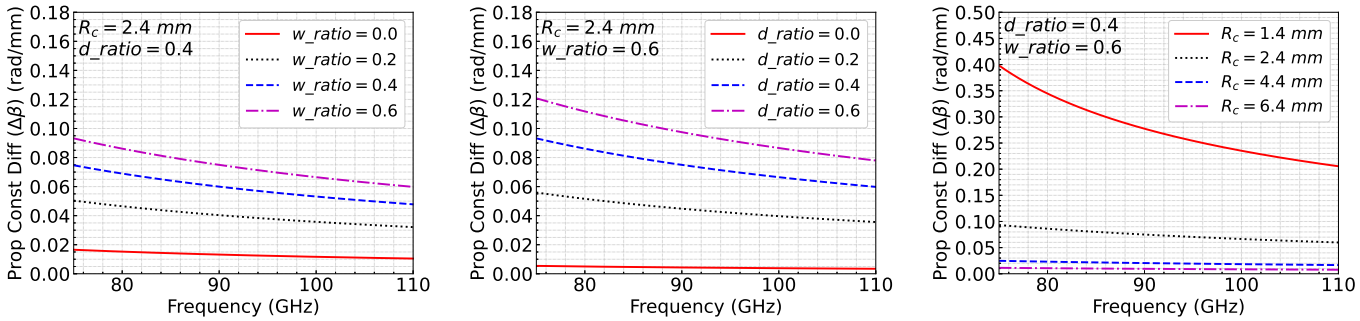

(a) (b) (c)

Fig. 5. Effect of the (a) groove width, (b) groove depth and (c) waveguide cross-section radius on the propagation constant difference ($\Delta\beta$) between the two orthogonal TE modes.

that

$$\begin{aligned}\Delta\phi_h(f) &= (\phi^0_{h_y} - \beta_{m1}(f)l) - (\phi^0_{h_x} - \beta_{m2}(f)l) \\ &= (\phi^0_{h_y} - \phi^0_{h_x}) - \Delta\beta(f)l \\ &= 0 - \pi/2 \\ &= -\pi/2.\end{aligned} \tag{3}$$

Therefore, an RHCP wave can be generated with the same grooved-wall circular waveguide dimension which leads to $\Delta\beta(f)l = \pi/2$ as that mentioned above, if the h-mode is used as the input.

Hence, it can be concluded that if the dimensions (r, d, w and l) of the grooved-wall circular waveguide are designed to give rise to a phase difference of $\pi/2$ between the two orthogonal degenerated modes, i.e., mode-1 and mode-2 shown in Fig. 2, both LHCP and RHCP can be generated by feeding the grooved-wall circular waveguide with TE_{11} modes which are oriented at $\pm 45°$ with respect to the grooves. This conclusion is also true for the multi-section grooved-wall horn, because it can be regarded as a concatenation of many discretized grooved-wall circular waveguides with various dimensions.

C. Parametric Study and Analysis

In this section, a parametric study has been performed on the groove depth and width as well as the circular waveguide radius of a grooved-wall circular waveguide with a uniform cross-section (see the inset of Fig. 2) by simulation in CST MWS, in order to find out the impact of these parameters on the CP performance. Because we are going to design a grooved-wall horn that has variable cross-section dimensions, we define the dimensions of the groove in a relative manner. Given the radius of the grooved-wall waveguide cross-section is R_c, the width and depth of the grooves is defined as

$$w = w_{min} + w\_ratio \cdot R_c \tag{4}$$

$$d = d\_ratio \cdot R_c \tag{5}$$

where w_min is the minimum width of the grooves and is set to 0.2 mm in our design.

Fig. 5(a) and Fig. 5(b) depict the effect of w_ratio and d_ratio on the propagation constant difference ($\Delta\beta$) between the two orthogonal degenerated TE modes respectively, when R_c is kept to 2.4 mm. The results show that, with a fixed R_c, larger w or d will result in larger $\Delta\beta$, which means shorter waveguide length will be needed to generate a CP wave. It can also be observed that groove depth will introduce larger $\Delta\beta$ than groove width with the same size. In Fig. 5(c), $\Delta\beta$ with different cross-section radius is shown when w_ratio and d_ratio are fixed to 0.6 and 0.4, respectively. It can be found that, with the same groove width ratio and groove depth ratio, the larger waveguide cross-section will lead to smaller $\Delta\beta$. In addition, all the results above show the frequency response of $\Delta\beta$ is not flat over the band. This uneven frequency response will limit the 3-dB AR bandwidth due to the phase error introduced after the two degenerated modes propagate over a certain distance.

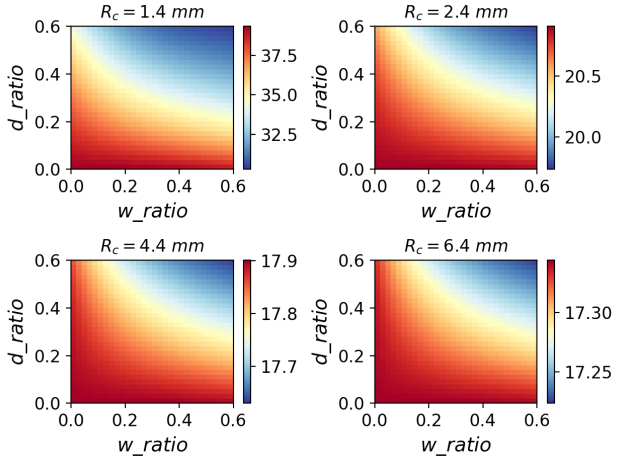

Fig. 6. Effect of the groove width and depth with different waveguide cross-section radii (R_c) on the maximum phase error (ϕ_e^{max}).

Fig. 6 illustrates the maximum phase error in degree over the expected operating bandwidth from 80 GHz to 110 GHz with the waveguide length that leads to the phase difference of 90° between the two orthogonal degenerated modes at the center frequency of 95 GHz. The ranges of w_ratio and d_ratio in this analysis are between 0 and 0.6. The maximum phase error in radian can be expressed as

$$\phi_e^{max} = \max_{f \in F}\{|\Delta\beta(f)l_0 - \pi/2|\}, F = \{f_l \le f \le f_r\} \tag{6a}$$

$$l_0 = (\pi/2)/\Delta\beta(f_c) \tag{6b}$$

where f_l =80 GHz, f_r = 110 GHz and f_c =90 GHz.

It can be found in Fig. 6 that larger groove width and depth will lead to smaller phase error hence wider AR bandwidth, and the phase error can be improved more by increasing the groove depth than by increasing the groove width. The reason for this is that, although the frequency response of $\Delta\beta$ is more even when groove width and depth is smaller, as shown in Fig. 5(a) and Fig. 5(b), the level of $\Delta\beta$ is so low that a much longer waveguide is needed to achieve 90° phase difference at the center frequency than the length needed when larger groove width and depth are used. As increasing groove width and depth will significantly increase the level of $\Delta\beta$ hence reducing the required waveguide length l_0 considerably, while the increment of $\Delta\beta(f)$ difference across the bandwidth is not as much as the decrease of l_0, ϕ_e^{max} can be lower when groove width and/or depth become larger. However, it should be pointed out that larger groove depth will cause narrower impedance bandwidth since the larger abrupt change in the waveguide structure is introduced, which implies that there will be a trade-off between impedance bandwidth and 3-dB AR bandwidth.

On the other hand, the result also shows that a larger cross-section radius will result in a lower phase error level (see the color bars next to each subfigure to find the phase error ranges of different cross-section radius). This means, not like reducing the groove depth and width, increasing waveguide cross-section radius will improve the flatness of the frequency response of $\Delta\beta$ so significantly that it can overcome the penalty introduced by larger waveguide length.

The analysis in this section suggests that a grooved-wall circular waveguide with flare-tapered cross-section and large groove widths should be designed to achieve wider overall bandwidth within a reasonable waveguide length in achieving a wideband CP horn.

III. Multi-section Grooved-wall CP Horn Design

A. Geometry Design

In the design of the N-section grooved-wall CP horn, dimensions of the $N+1$ cross-sections $(S_0, ..., S_N)$ of the grooved-wall waveguides will be decided first; then all cross-sections will be connected sequentially with linear transition. In our case, $N = 3$. The geometry of a grooved-wall CP horn with three linearly flared sections is presented in Fig. 7. In our design, the groove depth of the first cross-section is set to 0 in order to minimize the discontinuity between it and the input circular waveguide or the square-to-circular waveguide transformer. The groove depth of the last cross-section is also set to 0 so that the aperture will be close to a circle so that the amplitudes of the two orthogonal TE_{11} modes will be more balanced, as shown in our previous work [38].

The geometry of the grooved-wall multi-section horn is optimized using the Covariance Matrix Adaptation Evolution Strategy (CMA-ES) algorithm, which is proved to be promising in optimizing complicated EM devices in a self-adaptive way [42]. We have developed a Python software to control CST MWS full-wave simulations and analyze the result data exported from CST simulation automatically. A

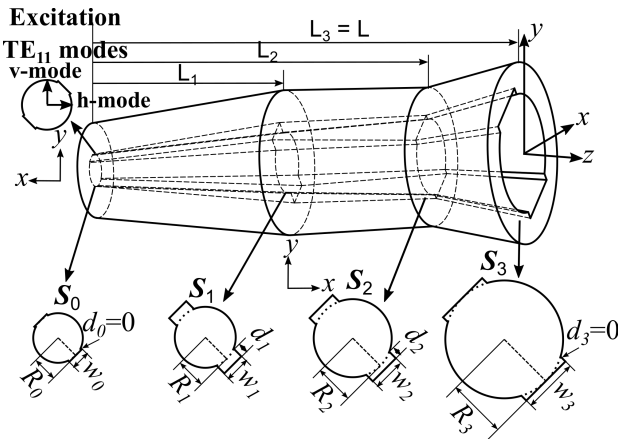

Fig. 7. Geometry of the multi-section grooved-wall CP horn.

TABLE I
THE OPTIMIZED DIMENSIONS OF THE MULTI-SECTION GROOVED-WALL HORN.

Parameters	L_0	L_1	L_2	L_3
Values (mm)	0	19.775	34.659	44.075
Parameters	$R_0(R_i)$	R_1	R_2	$R_3(R_o)$
Values (mm)	1.531	2.914	3.618	5.688
Parameters	d_0	d_1	d_2	d_3
Values (mm)	0	1	0	0
Parameters	w_0	w_1	w_2	w_3
Values (mm)	1.07	2.58	3.706	5.715

Python implementation of CMA-ES [43] is integrated into this software, so that the complete software is able to perform automatic CMA-ES optimization with full-wave simulations. Since we aim to achieve low reflection coefficients, AR $<$ 3 dB as well as rotationally symmetric radiation patterns with a low side-lobe level (SLL) over the entire operating bandwidth, a cost function including multiple objectives is defined. CMA-ES will try to minimize the value of the cost function to find the optimal design after a sufficient number of iterations. The optimized dimensions are shown in Table I.

B. Simulated Results of the Multi-Section Grooved-Wall CP Horn

The simulated reflection coefficients and AR of the optimized multi-section grooved-wall CP horn are shown in Fig. 8, where $|S1(v), 1(v)|$ is the reflection in v-mode (see Fig. 7) when input port is excited by v-mode which will affect the reflection coefficient of the complete dual-CP antenna, and $|S1(h), 1(v)|$ is the reflection in h-mode (see Fig. 7) when input port is excited by v-mode which will affect the isolation of the complete dual-CP antenna. It can be found that $|S1(v), 1(v)| < -42$ dB and $|S1(h), 1(v)| < -35$ dB is achieved over the desired operating bandwidth from 80 to 110 GHz. The AR is below 2.6 dB over the same bandwidth.

In order to investigate if higher-order modes excited in the flared sections of the optimized multi-section grooved-wall CP horn will affect the CP performance, mode analysis at the horn aperture is carried out using CST MWS. Fig. 9 shows

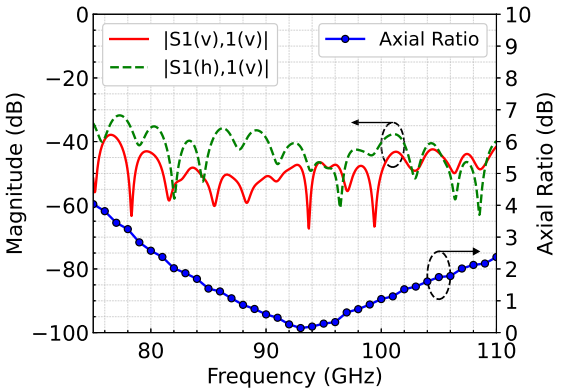

Fig. 8. Simulated S-parameters and AR of the optimized multi-section grooved-wall CP horn.

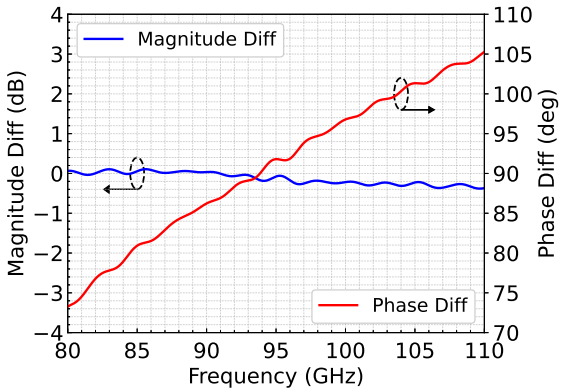

Fig. 10. Simulated magnitude and phase difference between x and y E-field components (E_x and E_y) of the LHCP wave in the farfield region when the input port of the optimized multi-section grooved wall horn is excited by v-mode. Magnitude difference (dB) is $|E_y| - |E_x|$.

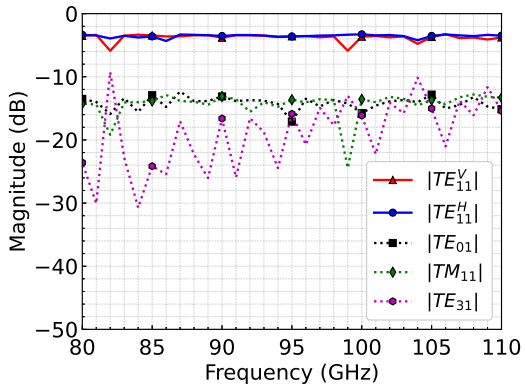

Fig. 9. Normalized magnitudes of the two orthogonal TE_{11} modes and the three largest higher-order modes at the aperture of the optimized grooved-wall CP horn.

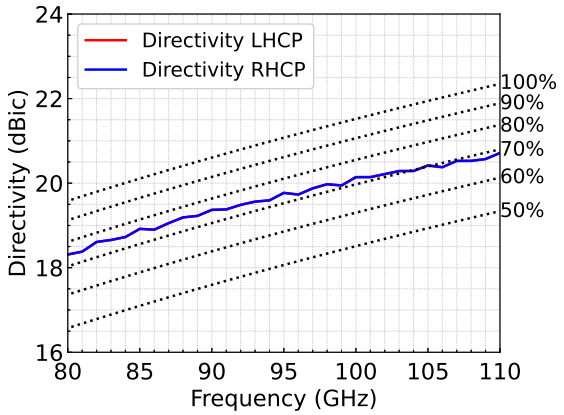

Fig. 11. Simulated directivity and aperture efficiency of the optimized grooved-wall CP horn.

the normalized magnitudes ($|S_{21}|$) of the two orthogonal degenerate TE_{11} modes (mode-1 and mode-2 in Fig. 2) and three largest higher-order modes at the horn aperture when the horn is excited by the vertical TE_{11} mode (v-mode in Fig. 7). It can be seen that the magnitudes of the two orthogonal degenerate TE_{11} modes (two orthogonal components of the CP wave) at the horn aperture are both kept around -3.5 dB and close to each other over the entire operating bandwidth from 80 - 110 GHz, which accounts for 89% of the total power. The three largest higher-order modes are TE_{01}, TM_{11} and TE_{31} modes. It can be observed that these higher-order modes are all well suppressed; their magnitudes are at least 10 dB lower than those of the two TE_{11} modes. The higher-order mode with the largest magnitude is TM_{11} mode, accounting for about 4% of the total power. TM_{11} mode is introduced at the aperture of the optimized horn because the addition of about 5% TM_{11} mode (with respect to 95% power of TE_{11} mode) to the dominant TE_{11} mode at the aperture can improve radiation patterns' symmetry, suppress cx-polarization and SLLs in comparison with the radiation performance generated by TE_{11} mode alone [44]. A larger proportion of TM_{11} mode (optimum is 15%) is required to further reduce the cx-polarization at the expense of narrow bandwidth and limited aperture efficiency due to the null in the far-field pattern of TM_{11} mode [44], [45].

Since the working principle of the proposed CP horn design relies on the manipulation of the dominant TE_{11} modes and the main objective is to achieve very low reflection coefficients over a wide bandwidth, the majority of the power is kept for TE_{11} modes in this design. It is also worth mentioning that the first two higher-order modes, TM_{01} and TE_{21} modes, are suppressed below -100 dB, so they are not shown in Fig. 9.

Fig. 10 depicts the magnitude and phase difference between the two orthogonal E-field components (E_x and E_y) of the LHCP wave at boresight in the farfield region when the input port is excited by v-mode. The result shows that the magnitudes of the two orthogonal components are very close to each other, and the phase difference is $90° \pm 15°$ within the frequency range of 80 - 110 GHz, which is acceptable according to several reported wideband dual-CP antennas [23]($88° \pm 20°$) and CP antennas [4]($90° \pm 15°$), [46]($90° \pm 10°$). Since AR is determined by both the magnitude difference and the phase difference [47], these results lead to an AR $<$ 2.6 dB as shown in Fig. 8, which meets the widely accepted standard of AR $<$ 3 dB for CP antennas [5]. The result for RHCP associated with the excitation of h-mode at the input port is the same due to the symmetry of the structure, except that the phase difference has an opposite sign.

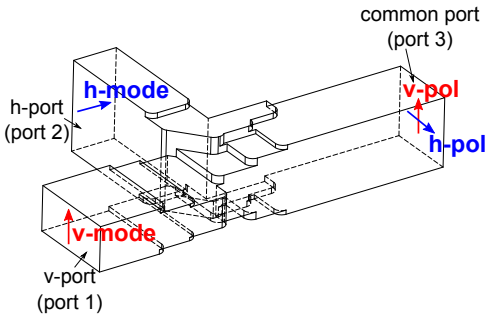

Fig. 12. Schematic of the asymmetric OMT used in this paper.

Another important performance of a multi-section smooth wall horn is the aperture efficiency. Typically, horn antennas have aperture efficiencies from 35% to 80% [47], and high aperture efficiency is desirable in certain applications such as horn arrays [45], [48]. Although the aperture efficiency was not one of the five optimization objectives (see Section III-A) and the main aim is to achieve very low reflection coefficients over a wide bandwidth, we verified that the optimized multi-section grooved-wall CP horn has an aperture efficiency at a moderate-high level, as presented in Fig. 11. It can be found that the aperture efficiency of the multi-section grooved-wall CP horn is from 74.6% to 68.7%.

IV. Orthomode Transducer Design

A. OMT Design

To realize the wideband dual-CP antenna with high isolation based on the grooved-wall CP horn in Section III, a wideband OMT with high isolation is required. Although the symmetric OMTs such as [49] and [50] could be a better choice as they offer wider bandwidth and better matching and isolation level, their structures are complicated for fabrication, which also limits their capability to scale up to even higher frequencies. Since we aim to demonstrate the dual-CP capability of our grooved-wall CP horn and show its potential to be scaled up to higher frequencies, the asymmetric OMT in [41] was chosen, which has been scaled up to over 600 GHz [51], [52].

The geometry of the OMT we used in this paper is shown in Fig. 12. The vertical polarization in the common port (port 3) is guided to the v-port (port 1) which is in line with the common port, while the horizontal polarization is extracted to the h-port (port 2) by using a T-shaped waveguide. This design is based on the designs presented in [41], [51], but with a critical modification that can resolve a major issue of this type of OMT.

In [41] and [51], the OMTs are split horizontally into two block halves in the middle of the common port in fabrication, as shown in Fig. 13(a). However, it is noted in [41], [51] that the polarization isolation is very sensitive to the misalignment between the upper and lower block halves, and the reason is explained in [41]. According to the analysis in [41], the polarization isolation will deteriorate to 22 dB when the misalignment is 7 μm in W-band.

In order to mitigate degradation of the cross-polarization level caused by this misalignment error and achieve high

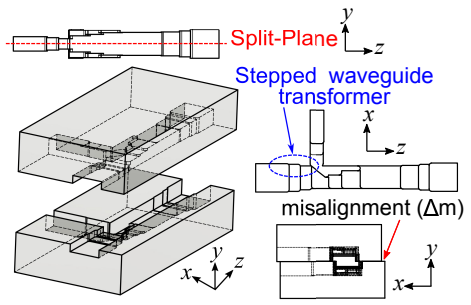

(a) Horizontal-split blocks in [41].

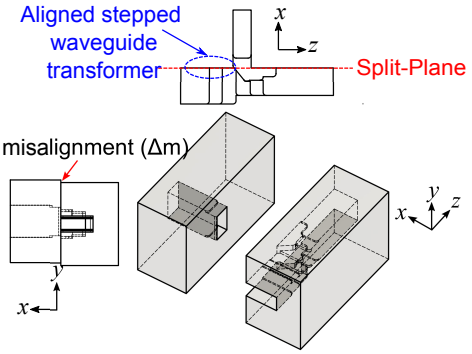

(b) Vertical-split blocks propsed in this paper.

Fig. 13. OMT split-block design (a) in [41] and (b) proposed in this paper.

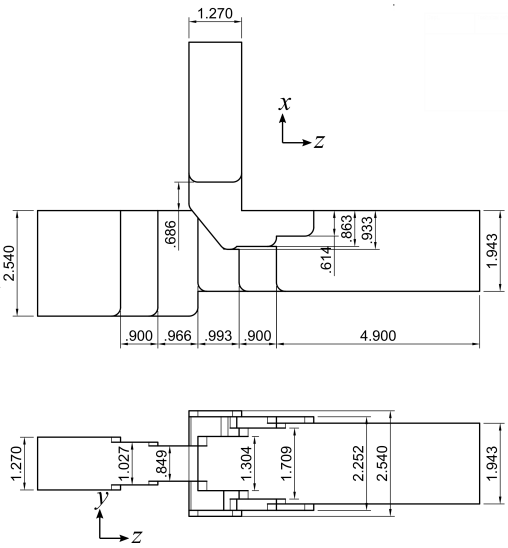

Fig. 14. Dimensions of the optimized OMT.

polarization and port isolation, we have modified the OMT design in [41] so that the stepped waveguide transformer to the v-port is aligned with the T-junction waveguide on the side of the h-port arm, which is illustrated in Fig. 13(b). This modification allows the OMT to be split on the aligned side of the axial part of the OMT, which prevents the cross-section of the axial waveguide to the common port from being changed if there is a misalignment between two splitting blocks during assembling, as shown in Fig. 13(b).

The OMT design is optimized using CST MWS to cover the frequency range from 80 - 110 GHz with expected polarization and port isolation larger than 50 dB. The optimized dimensions

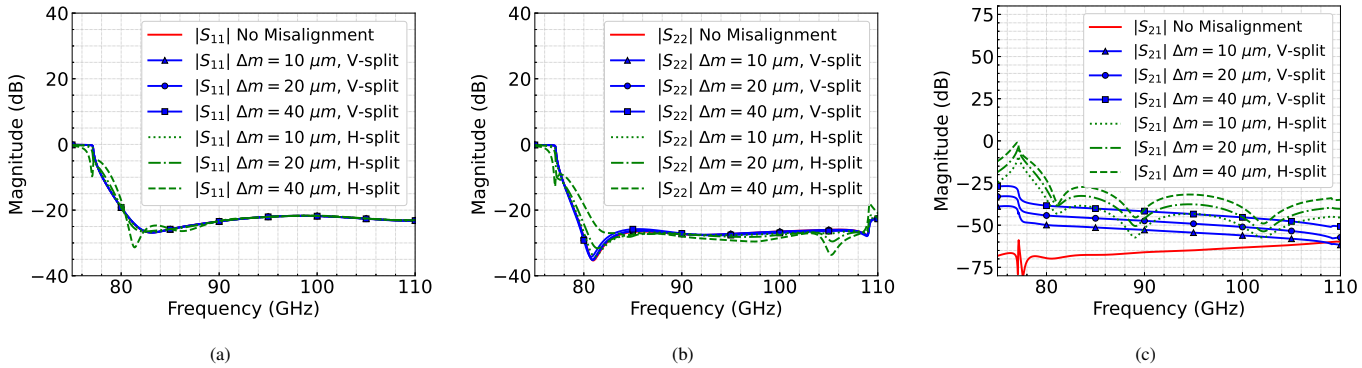

Fig. 15. Reflection coefficients for (a) port 1 and (b) port 2, and (c) port isolation when port 1 is excited.

of the OMT are presented in Fig. 14.

B. OMT Simulation Results

The full-wave simulation of the proposed OMT is carried out using CST MWS. The reflection coefficients, port isolation and polarization isolation of the proposed OMT are shown in Fig. 15 to Fig. 16. The impact on these characteristics caused by the misalignment shown in Fig. 13(a) and Fig. 13(b) is also presented to demonstrate the improvement for misalignment tolerance resulted from the modification we introduced.

It can be observed from Fig. 15(a) and Fig. 15(b) that the reflection coefficients for both port 1 and 2 are below 20 dB, and there is no noticeable impact on the reflection coefficients for both port 1 and port 2 if the misalignment is within 40 μm when the splitting approach we proposed is applied. On the other hand, the reflection coefficient at two ends of the operating bandwidth deteriorates when horizontal splitting is applied, and the misalignment reaches 40 μm.

In Fig. 15(c), it can be seen that the port isolation is lower than 60 dB for port 1, and will decrease as the misalignment between two vertical-split blocks increases, but can still be kept higher than 40 dB from 80 GHz to 110 GHz if the misalignment is smaller than 40 μm. However, when the misalignment increases to 40 μm, the port isolation level decreases to 25 dB at 80 GHz if the proposed OMT is horizontally split into two block halves. Only $|S_{21}|$ is shown here because $|S_{12}|$ is the same as $|S_{21}|$ due to the symmetry of port isolation in the simulation.

Fig. 16 depicts the polarization isolation level for vertical and horizontal polarization, where $|S3(h), 1(v)|$ denotes the cross-polarization (horizontal polarization) level at port 3 when port 1 is excited, and $|S3(v), 1(h)|$ denotes the cross-polarization (vertical polarization) level at port 3 when port 2 is excited. It can be found that the polarization isolation $>$ 50 dB is achieved. Significant degradation of polarization can be observed if the OMT is horizontally split, the polarization isolation decreases to 20 dB at the lower end of the expected operating bandwidth even with only 10 μm misalignment, which is also consistent with the analysis result presented in [41]. By contrast, the polarization isolation can still be kept above 35 dB even if the misalignment increases up to 40 μm when the OMT is vertically split as we proposed.

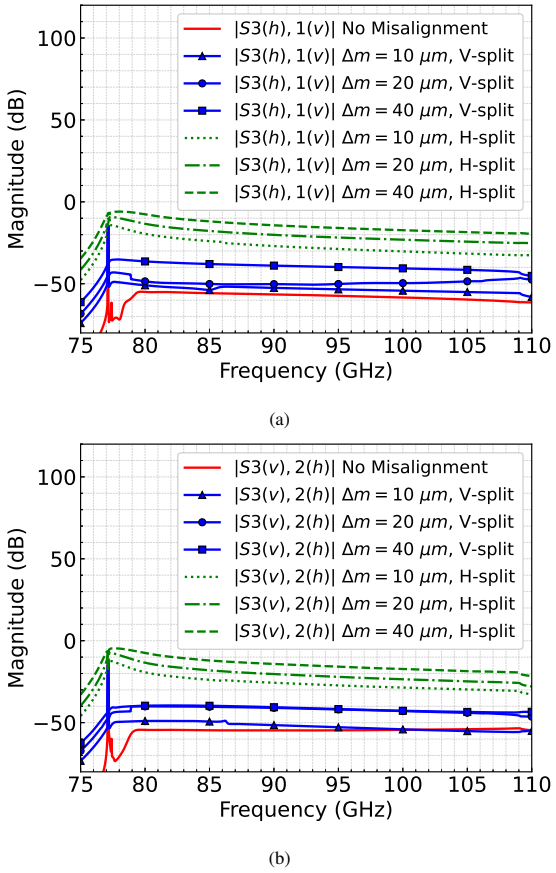

Fig. 16. Polarization isolation for (a) vertical polarization (when port 1 is excited) and (b) horizontal polarization (when port 2 is excited).

Therefore, the simulated results show that, by using our design, a significant improvement in port isolation and polarization isolation can be achieved when there is a misalignment between 2 split blocks during assembling.

V. Measurement of the Complete Dual-CP Antenna and Discussion

A. Simulated and Measured Results

Full-wave simulation of the complete dual-CP antenna shown in Fig. 1 is performed using CST MWS.

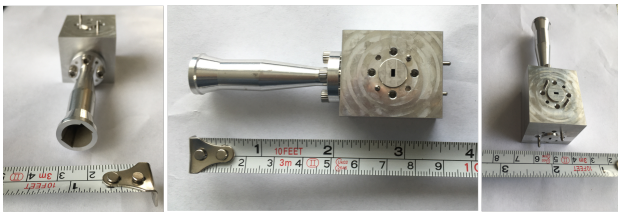

Fig. 17. Photograph of the prototype of the proposed dual-CP antenna.

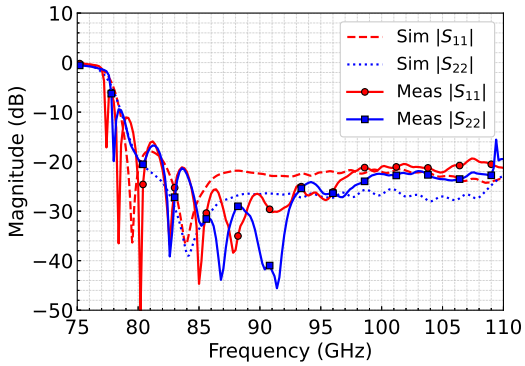

(a)

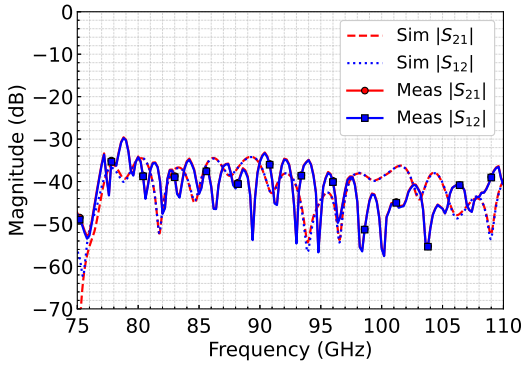

(b)

Fig. 18. Measured and simulated (a) Reflection coefficient and (b) Isolation of the proposed dual-CP antenna.

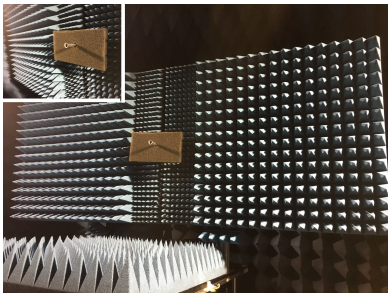

Fig. 19. Photograph of CATR measurement setup.

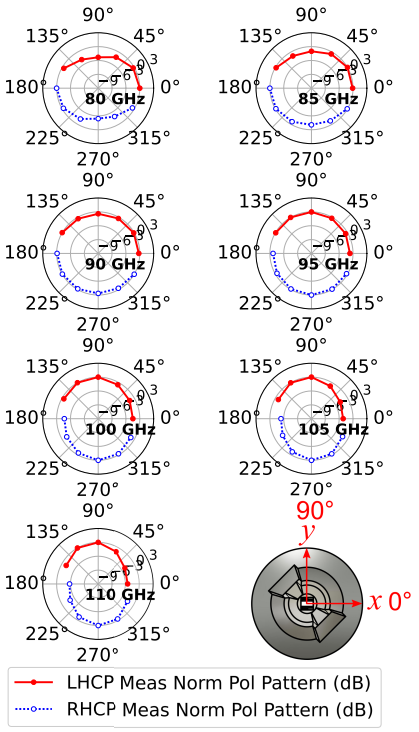

Fig. 20. Measured polarization patterns of the proposed dual-CP antenna at several frequencies within the frequency range from 80 to 110 GHz.

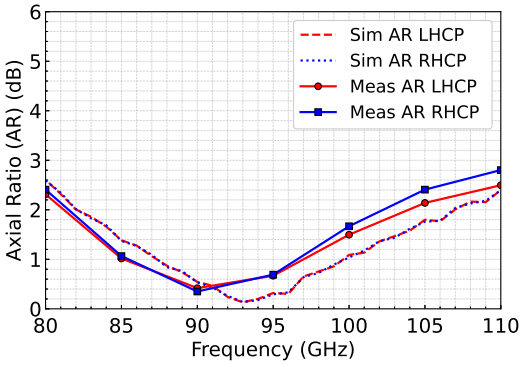

Fig. 21. Measured and simulated AR of the proposed dual-CP antenna over the frequency range from 80 to 110 GHz.

A prototype of the proposed dual-CP antenna working in the W-band is fabricated, and a photograph of the prototype is shown in Fig. 17. The multi-section grooved-wall horn and the square-to-circular waveguide transformer is fabricated as one piece using spark erosion rather than two split-block halves using CNC milling, because the misalignment of two halves during assembling will significantly degrade the AR as discussed in [32]. The OMT is split into two blocks as illustrated in Fig. 13(b), and is fabricated using spark erosion and CNC milling. The spark erosion is applied to fabricate the T-shaped junction of the OMT so that all the steps and round corners in the design can be fabricated. The waveguide sections without steps are fabricated using CNC milling. The horn with the square-to-circular waveguide transformer is then assembled with the OMT via UG387 flanges.

The scattering parameters measurement of the dual-CP antenna is performed using a Keysight PNA-X network analyzer with two OML WR-10 extension heads. The measured and simulated reflection coefficients and port isolation of the dual-CP antenna are shown in Fig. 18. It can be found from Fig. 18(a) that the reflection coefficients of both port 1 and port 2 are below -20 dB over most of the frequency range from 80 GHz to 110 GHz, they only deteriorate to -16 dB around

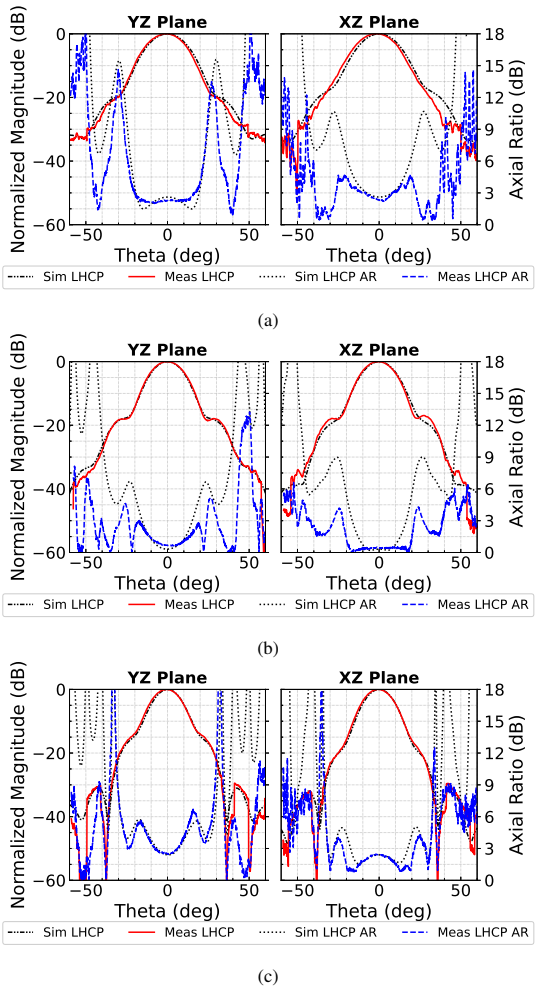

Fig. 22. Normalized measured and simulated LHCP (port 1 excited) radiation patterns of the proposed dual-CP antenna at (a) 80 GHz, (b) 95 GHz and (c) 110 GHz.

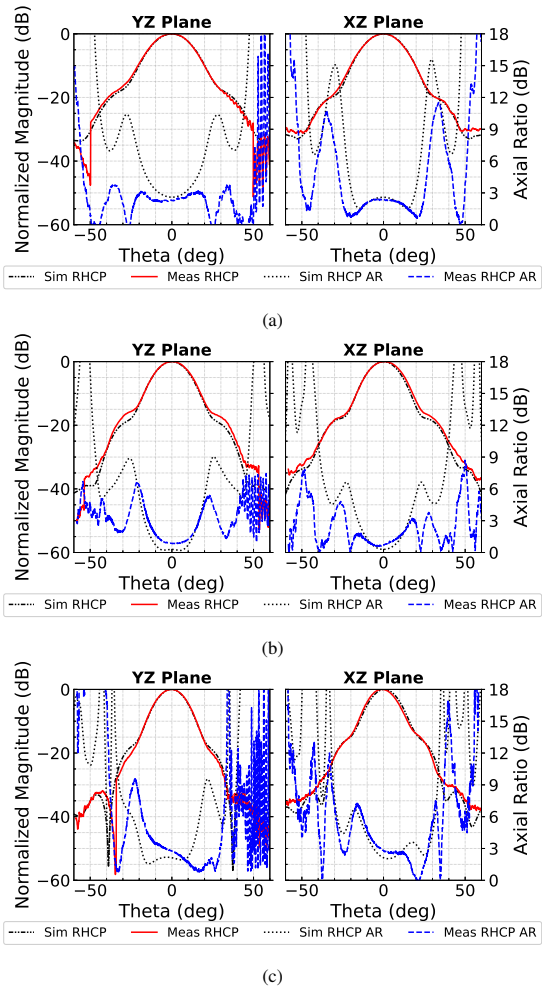

Fig. 23. Normalized measured and simulated RHCP (port 2 excited) radiation patterns of the proposed dual-CP antenna at (a) 80 GHz, (b) 95 GHz and (c) 110 GHz.

82.5 GHz, and the measured results are close to the simulated ones. According to Fig. 18(b), measured $|S_{21}|$ and $|S_{12}|$ are both lower than -32.5 dB over the frequency range from 80 GHz to 110 GHz, which agrees well with the simulated results. Therefore, port isolation higher than 32.5 dB is achieved over a bandwidth of 31.6%.

The radiation characteristics are measured using a mmWave Compact Antenna Test Range (CATR) in the Antenna Lab at Queen Mary University of London. The photograph of the CATR measurement setup for the proposed dual-CP antenna is shown in Fig. 19. In the mmWave CATR, a W-band linearly-polarized corrugated horn is connected to a motor and installed in the CATR as a reference feed antenna, which can be rotated to an arbitrary angle within 360° along its center axis, so that the magnitudes of different polarization components of Antenna Under Test (AUT) can be measured. In this measurement, the rotation angle of the reference antenna is set from 0° to 150° with a step of 30° to measure 6 polarization components, which is proved to be sufficient to find the major and minor axes of the polarization ellipse of this antenna. For each angle, the AUT mounted on a positioner is scanned horizontally to measure the magnitudes with respect to azimuth (θ) for this polarization components. After that, the polarization components with maximum and minimum magnitudes at $\theta = 0°$ (boresight) are considered as the major and minor axes of the polarization ellipse, respectively. The ratio of the maximum to minimum magnitude defines the AR at the boresight of the AUT. By calculating the difference between these two selected curves, AR with respect to θ can also be obtained.

According to the obtained AR with respect to azimuth (θ), cross-polarization discrimination (XPD) with respect to azimuth (θ) can be derived, and together with total radiation derived from magnitudes of major and minor axes of the polarization ellipse, the LHCP/RHCP components can be calculated.

The normalized measured polarization patterns [53] of the proposed dual-CP antenna at several frequencies across the expected operating bandwidth from 80 GHz to 110 GHz are illustrated in Fig. 20, which reveals the CP characteristics of the proposed dual-CP antenna. The coordinate system in Fig. 20 follows that in Fig. 1. As can be seen from the figure, the polarization patterns at the middle frequencies are closer to circles than those at the edge frequencies, which implies

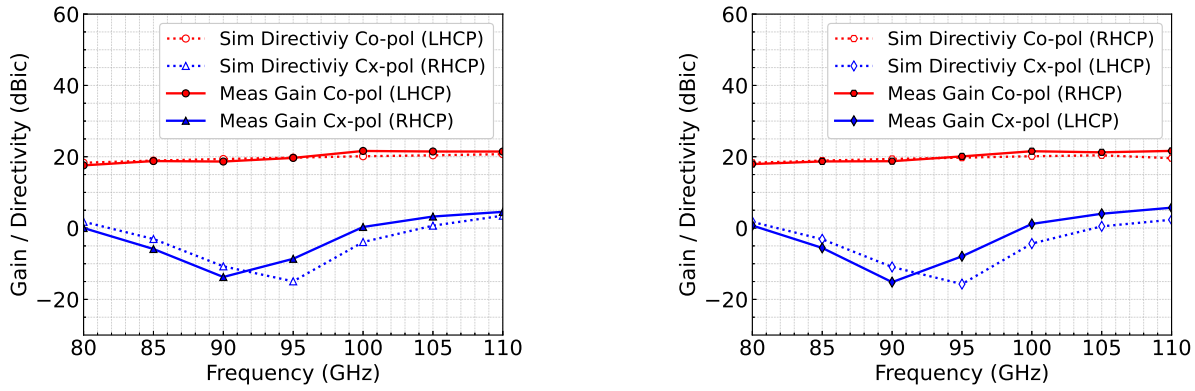

(a) (b)

Fig. 24. Measured gain and simulated directivity of co-pol and cx-pol at boresight over the entire operating bandwidth for (a) LHCP (port 1 excitation) and (b) RHCP (port 2 excitation).

TABLE II
COMPARISON WITH OTHER DUAL-CP ANTENNAS BASED ON WAVEGUIDE STRUCTURES.

Ref	Frequency (GHz)	Type	Reflection Coefficient (dB)	Isolation (dB)	AR (dB)	Overall Band-width	Max Gain (dBic)	Antenna Length	Year
[26]	1.27 - 1.32	Septum polarizer + Horn	<-25	>30	<1*	3.9%	–	$4.3\lambda_0$	2011
[27]	1.57542	Septum polarizer + Horn	<-29.3	>23	<0.023	1.0%	16.2	$5.44\lambda_0$	2016
[28]	8 - 8.5	Septum polarizer array	<-15	>20	<0.7	13.0%	8	$\sim 1.76\lambda_0$	2009
[30]	28.5 - 31.2	Septum polarizer + Horn	<-25	>27	<0.7	9.0%	–	$12.5\lambda_0$	2018
[31]	27.6 - 32.4	Septum polarizer + Waveguide array	<-10	>13	<3	16.0%	32.8	$5.1\lambda_0$	2017
[39]	53.71 - 58.1	Mono-Groove Polarizer + Horn	<-10	>15*	<2.2	7.9%	12	$7.5\lambda_0$	2020
[32]	76.8 - 94.7	Septum polarizer + Horn	<-15	>20	<5.8	20.9%	20.3	$16.4\lambda_0$	2019
[33]	213 - 237	Septum polarizer + Horn	<-21	>30	<1.5	10.0%	22**	–	2013
This work	80 - 110	Multi-section grooved-wall CP horn + OMT	<-20	>32.5	<2.8	31.6%	21.6	$21.6\lambda_0$	2020

* Simulated results.
** Simulated results of the linearly-polarized horn.

good AR is achieved in the middle of the expected working bandwidth, and AR deteriorates at the two ends of the expected working bandwidth. It can also be observed that the major axes of the polarization ellipses deviate from $x-$ and $y-$axis (0° and 90°), which means the phase difference shifts away from 90° when the frequency goes towards the low and high ends of the operating bandwidth and is consistent with the simulated result shown in Fig. 10.

Fig. 21 depicts the measured AR derived from the aforementioned measuring approach and the polarization patterns. The result shows that the measured AR of both LHCP and RHCP are below 2.8 dB from 80 GHz to 110 GHz. It can also be observed that the measured AR slightly shifts left from the simulated AR. This small discrepancy is probably due to the fabrication error of the horn and groove dimensions, which will cause the phase difference between the two orthogonal components of the generated CP wave to deviate from that in design.

Therefore, taking the impedance and AR bandwidth into account, the overall operating bandwidth of 31.6% (80 - 110 GHz) is achieved for the proposed dual-CP antenna with port isolation $>$ 32.5 dB and AR $<$ 2.8 dB. In fact, the overall operating bandwidth is limited by the reflection coefficient of the OMT.

The normalized measured and simulated radiation patterns of LHCP and RHCP within $\pm 60^\circ$ in the $yz-$ and $xz-$plane (see Fig. 1) at 80 GHz, 95 GHz and 110 GHz are presented in Fig. 22 and Fig. 23. AR with respect to θ is also shown in the figures. The measured radiation patterns agree well with the simulated ones. It can be found that a good rotational symmetry is achieved for the main lobes at all frequencies, allowing this dual-CP antenna to be used as a feed to a reflector antennas if higher gain is required. Sidelobe level (SLL) lower than -30 dB is also observed.

Fig. 24(a) and Fig. 24(b) show the measured gain and simulated directivity of co-pol and cx-pol at boresight over the entire operating bandwidth for LHCP (port 1 excitation) and RHCP (port 2 excitation), respectively. The result shows that the co-pol gain of LHCP is from 17.6 dBic to 21.6 dBic, and the co-pol gain of RHCP is from 17.9 dBic to 21.6 dBic. It can also be derived from the figure that the best cross-polarization discrimination (XPD) is around 34 dB, while the worst case is about 17 dB for RHCP within the operating bandwidth. All the results agree well with the simulated ones.

B. Comparison and Discussion

The performance of other reported dual-CP antennas based on waveguide structures are summarized in Table II in comparison with the results of the dual-CP antenna proposed in this paper. The overall bandwidth in the table describes the overlapped bandwidth for the impedance and AR. λ_0 is the wavelength in free space at the center frequency. It can be found that our design shows the highest isolation over the widest bandwidth among all dual-CP antennas ever reported. In comparison with the design presented in [39] consisting of the mono-groove polarizer and horn, our design shows significantly higher isolation over a wider bandwidth with lower reflection coefficient and similar AR, as well as higher gain. When compared with the designs based on the septum polarizer and horn, our design with a septum-free structure not only has higher isolation over wider bandwidth, but also can be scaled up to THz band. However, it should be noted that the antenna length of our design is longer than others. The reason for this lies in the fact that the grooved-wall horn achieves wide AR bandwidth at the expense of longer groove length, as explained in Section II-B. Additionally, a relatively long ($3.33\lambda_0$) smooth square-to-circular waveguide transition is used instead of a stepped waveguide transition because it can achieve a low reflection over a wider bandwidth at the expense of longer length [44]. Although the wideband OMT with a circular waveguide common port, such as [49], can be used to avoid the square-to-circular waveguide transition hence reducing the overall length, the OMT design based on a T-shaped junction is chosen because it has a hollow waveguide structure and has been scaled up to THz band.

VI. Conclusion

This paper presents a new type of dual-CP antenna is presented, which is based on a multiple-section grooved-wall CP antenna and an improved OMT. The multiple-section grooved-wall CP antenna consisting of multiple conical sections has a pair of grooves with variable depth and width on the walls of each section, which serves as an inbuilt polarizer to generate CP. This CP antenna is demonstrated to be able to generate dual-CP with the operating principle being illustrated. A prototype of the proposed dual-CP antenna working in the W-band is designed in simulation and verified in experimental measurement. The simulated and measured results are in good agreement, showing that a 31.6% bandwidth ranging from 80 GHz to 110 GHz is achieved with reflection coefficient $<$ -20 dB and port isolation $>$ 32.5 dB as well as AR $<$ 2.8 dB for both LHCP and RHCP. A high gain of 19.6 ± 2 dBic is realized for both LHCP and RHCP over the entire operating bandwidth. Rotationally symmetric radiation patterns are also observed with the SLL lower than -30 dB. To the best of the authors' knowledge, this is the dual-CP antenna with the highest isolation over the widest bandwidth ever reported among all dual-CP antennas. Furthermore, with a septum-free structure, this type of dual-CP antenna has the potential to be scaled up to even THz band.

Acknowledgment

The authors would like to thank Dr. Max Munoz Torrico from Antenna Lab at Queen Mary University of London for calibrating the mmWave CATR, as well as his valuable help with the measurement. This research utilized Queen Mary's Apocrita HPC facility, supported by QMUL Research-IT [54].

References

[1] Y. He, C. Gu, H. Ma, J. Zhu, and G. V. Eleftheriades, "Miniaturized Circularly Polarized Doppler Radar for Human Vital Sign Detection," *IEEE Trans. Antennas Propag.*, vol. 67, no. 11, pp. 7022–7030, 2019.

[2] X. Chen, C. G. Parini, B. Collins, Y. Yao, and M. Ur Rehman, *Antennas for Global Navigation Satellite Systems*. Chichester, UK: John Wiley & Sons, Ltd, 3 2012.

[3] C. Mao, S. Gao, Y. Wang, Q. Chu, and X. Yang, "Dual-Band Circularly Polarized Shared-Aperture Array for C -/ X -Band Satellite Communications," *IEEE Trans. Antennas Propag.*, vol. 65, no. 10, pp. 5171–5178, 2017.

[4] G. Mishra, S. K. Sharma, and J. S. Chieh, "A Circular Polarized Feed Horn With Inbuilt Polarizer for Offset Reflector Antenna for W-Band CubeSat Applications," *IEEE Trans. Antennas Propag.*, vol. 67, no. 3, pp. 1904–1909, 2019.

[5] S. Gao, Q. Luo, and F. Zhu, *Circularly Polarized Antennas*. Chichester, UK: John Wiley & Sons, Ltd, 1 2014.

[6] Y. Yao, X. Cheng, C. Wang, J. Yu, and X. Chen, "Wideband Circularly Polarized Antipodal Curvedly Tapered Slot Antenna Array for 5G Applications," *IEEE J. Sel. Areas Commun.*, vol. 35, no. 7, pp. 1539–1549, 2017.

[7] X. Li, J. Xiao, and J. Yu, "Long-Distance Wireless mm-Wave Signal Delivery at W-Band," *J. Lightw. Technol.*, vol. 34, no. 2, pp. 661–668, 2016.

[8] X. Li, J. Yu, K. Wang, Y. Xu, L. Chen, L. Zhao, and W. Zhou, "Delivery of 54-Gb/s 8QAM W-Band Signal and 32-Gb/s 16QAM K -Band Signal Over 20-km SMF-28 and 2500-m Wireless Distance," *J. Lightw. Technol.*, vol. 36, no. 1, pp. 50–56, 2018.

[9] K. Brown, A. Brown, T. Feenstra, D. Gritters, E. Ko, S. O'Connor, M. Sotelo, and Raytheon, "Long-range wireless link with fiber-equivalent data rate," in *2017 IEEE MTT-S International Microwave Symposium (IMS)*, 2017, pp. 809–811.

[10] A. Sabharwal, P. Schniter, D. Guo, D. W. Bliss, S. Rangarajan, and R. Wichman, "In-Band Full-Duplex Wireless: Challenges and Opportunities," *IEEE J. Sel. Areas Commun.*, vol. 32, no. 9, pp. 1637–1652, 2014.

[11] J. Wu, M. Li, and N. Behdad, "A Wideband, Unidirectional Circularly Polarized Antenna for Full-Duplex Applications," *IEEE Trans. Antennas Propag.*, vol. 66, no. 3, pp. 1559–1563, 2018.

[12] H. Nawaz, A. U. Niazi, M. Abdul Basit, and M. Usman, "Single Layer, Differentially Driven, LHCP Antenna With Improved Isolation for Full Duplex Wireless Applications," *IEEE Access*, vol. 7, pp. 169 796–169 806, 2019.

[13] Y. Shen, S. Zhou, G. Huang, and T. Chio, "A Compact Dual Circularly Polarized Microstrip Patch Array With Interlaced Sequentially Rotated Feed," *IEEE Trans. Antennas Propag.*, vol. 64, no. 11, pp. 4933–4936, 2016.

[14] C. Mao, S. S. Gao, Y. Wang, and J. T. Sri Sumantyo, "Compact Broadband Dual-Sense Circularly Polarized Microstrip Antenna/Array With Enhanced Isolation," *IEEE Trans. Antennas Propag.*, vol. 65, no. 12, pp. 7073–7082, 2017.

[15] A. Garcia-Aguilar, J. Inclan-Alonso, L. Vigil-Herrero, J. Fernandez-Gonzalez, and M. Sierra-Perez, "Low-Profile Dual Circularly Polarized Antenna Array for Satellite Communications in the X Band," *IEEE Trans. Antennas Propag.*, vol. 60, no. 5, pp. 2276–2284, 2012.

[16] Y. Yang, J. Guo, B. Sun, Y. Cai, and G. Zhou, "The Design of Dual Circularly Polarized Series-Fed Arrays," *IEEE Trans. Antennas Propag.*, vol. 67, no. 1, pp. 574–579, 2019.

[17] Q. Luo, S. Gao, M. Sobhy, J. T. Sri Sumantyo, J. Li, G. Wei, J. Xu, and C. Wu, "Dual Circularly Polarized Equilateral Triangular Patch Array," *IEEE Trans. Antennas Propag.*, vol. 64, no. 6, pp. 2255–2262, 2016.

[18] Y. Yang, B. Sun, and J. Guo, "A Low-Cost, Single-Layer, Dual Circularly Polarized Antenna for Millimeter-Wave Applications," *IEEE Antennas Wireless Propag. Lett.*, vol. 18, no. 4, pp. 651–655, 2019.

[19] A. T. Pereda, F. Caminita, E. Martini, I. Ederra, J. Teniente, J. C. Iriarte, R. Gonzalo, and S. Maci, "Experimental Validation of a Ku-Band Dual-Circularly Polarized Metasurface Antenna," *IEEE Trans. Antennas Propag.*, vol. 66, no. 3, pp. 1153–1159, 2018.

[20] Y. Cai, Y. Zhang, Z. Qian, W. Cao, and S. Shi, "Compact Wideband Dual Circularly Polarized Substrate Integrated Waveguide Horn Antenna," *IEEE Trans. Antennas Propag.*, vol. 64, no. 7, pp. 3184–3189, 2016.

[21] Q. Wu, J. Hirokawa, J. Yin, C. Yu, H. Wang, and W. Hong, "Millimeter-Wave Multibeam Endfire Dual-Circularly Polarized Antenna Array for 5G Wireless Applications," *IEEE Trans. Antennas Propag.*, vol. 66, no. 9, pp. 4930–4935, 2018.

[22] J. Xu, W. Hong, Z. H. Jiang, J. Chen, and H. Zhang, "A Q-Band Low-Profile Dual Circularly Polarized Array Antenna Incorporating Linearly Polarized Substrate Integrated Waveguide-Fed Patch Subarrays," *IEEE Trans. Antennas Propag.*, vol. 65, no. 10, pp. 5200–5210, 2017.

[23] Y. Zhao and K. Luk, "Dual Circular-Polarized SIW-Fed High-Gain Scalable Antenna Array for 60 GHz Applications," *IEEE Trans. Antennas Propag.*, vol. 66, no. 3, pp. 1288–1298, 2018.

[24] Y. J. Cheng, J. Wang, and X. L. Liu, "94 GHz Substrate Integrated Waveguide Dual-Circular-Polarization Shared-Aperture Parallel-Plate Long-Slot Array Antenna With Low Sidelobe Level," *IEEE Trans. Antennas Propag.*, vol. 65, no. 11, pp. 5855–5861, 2017.

[25] M. Chen and G. Tsandoulas, "A wide-band square-waveguide array polarizer," *IEEE Trans. Antennas Propag.*, vol. 21, no. 3, pp. 389–391, 1973.

[26] M. J. Franco, "A High-Performance Dual-Mode Feed Horn for Parabolic Reflectors with a Stepped-Septum Polarizer in a Circular Waveguide [Antenna Designer's Notebook]," *IEEE Antennas Propag. Mag.*, vol. 53, no. 3, pp. 142–146, 2011.

[27] M. Mrnka, M. Pavlovic, and Z. Raida, "Antenna Range Illuminator Based on a Septum Polarizer and a Dual-Mode Horn [Measurements Corner]," *IEEE Antennas Propag. Mag.*, vol. 58, no. 4, pp. 82–86, 2016.

[28] C. Kumar, V. V. Srinivasan, V. K. Lakshmeesha, and S. Pal, "Novel Dual Circularly Polarized Radiating Element for Spherical Phased-Array Application," *IEEE Antennas Wireless Propag. Lett.*, vol. 8, pp. 826–829, 2009.

[29] G. Jazani and A. Pirhadi, "Design of dual-polarised (RHCP/LHCP) quad-ridged horn antenna with wideband septum polariser waveguide feed," *IET Microw., Antennas & Propag.*, vol. 12, no. 9, pp. 1541–1545, 2018.

[30] G. Addamo, O. A. Peverini, D. Manfredi, F. Calignano, F. Paonessa, G. Virone, R. Tascone, and G. Dassano, "Additive Manufacturing of Ka-Band Dual-Polarization Waveguide Components," *IEEE Trans. Microw. Theory Techn.*, vol. 66, no. 8, pp. 3589–3596, 2018.

[31] J. Wu, Y. J. Cheng, H. B. Wang, Y. C. Zhong, D. Ma, and Y. Fan, "A Wideband Dual Circularly Polarized Full-Corporate Waveguide Array Antenna Fed by Triple-Resonant Cavities," *IEEE Trans. Antennas Propag.*, vol. 65, no. 4, pp. 2135–2139, 4 2017.

[32] C. Shu, J. Wang, S. Hu, Y. Yao, J. Yu, Y. Alfadhl, and X. Chen, "A Wideband Dual-Circular-Polarization Horn Antenna for mmWave Wireless Communications," *IEEE Antennas Wireless Propag. Lett.*, vol. 18, no. 9, pp. 1726–1730, 9 2019.

[33] C. A. Leal-Sevillano, K. B. Cooper, J. A. Ruiz-Cruz, J. R. Montejo-Garai, and J. M. Rebollar, "A 225 GHz Circular Polarization Waveguide Duplexer Based on a Septum Orthomode Transducer Polarizer," *IEEE Trans. THz Sci. Technol.*, vol. 3, no. 5, pp. 574–583, 2013.

[34] B. Deutschmann and A. F. Jacob, "Broadband Septum Polarizer With Triangular Common Port," *IEEE Trans. Microw. Theory Techn.*, pp. 1–8, 2019.

[35] U. Tucholke, F. Arndt, and T. Wriedt, "Field Theory Design of Square Waveguide Iris Polarizers," *IEEE Trans. Microw. Theory Techn.*, vol. 34, no. 1, pp. 156–160, 1986.

[36] G. Virone, R. Tascone, O. A. Peverini, G. Addamo, and R. Orta, "Combined-Phase-Shift Waveguide Polarizer," *IEEE Microw. Wireless Compon. Lett.*, vol. 18, no. 8, pp. 509–511, 2008.

[37] C. Shu, S. Hu, Y. Yao, and X. Chen, "A W-band Compact Circularly Polarized Horn Antenna," in *2019 12th UK-Europe-China Workshop on Millimetre Waves and Terahertz Technologies (UCMMT)*, 2019.

[38] C. Shu, S. Hu, Y. Yao, Y. Alfadhl, and X. Chen, "W-band grooved-wall circularly polarised horn antenna," *IET Microw., Antennas & Propag.*, vol. 14, no. 11, pp. 1171–1174, 2020.

[39] N. Luo, X. Yu, G. Mishra, and S. K. Sharma, "A Millimeter-Wave (V-Band) Dual-Circular-Polarized Horn Antenna Based on an Inbuilt Monogroove Polarizer," *IEEE Antennas Wireless Propag. Lett.*, vol. 19, no. 11, pp. 1933–1937, 2020.

[40] C. Shu, "Wideband dual-circular-polarization antennas for millimetre-wave wireless communications," Ph.D. dissertation, Queen Mary Univ. of London, London, July 2021.

[41] A. Dunning, S. Srikanth, and A. R. Kerr, "A simple orthomode transducer for centimeter to submillimeter wavelengths," in *20th International Symposium on Space Terahertz Technology*, Charlottesville, USA, 2009, pp. 191–193.

[42] M. D. Gregory, Z. Bayraktar, and D. H. Werner, "Fast Optimization of Electromagnetic Design Problems Using the Covariance Matrix Adaptation Evolutionary Strategy," *IEEE Trans. Antennas Propag.*, vol. 59, no. 4, pp. 1275–1285, 2011.

[43] Y. A. Nikolaus Hansen and P. Baudis, "pycma version 2.7.0," 2019. [Online]. Available: https://github.com/CMA-ES/pycma

[44] A. D. Olver, P. J. B. Clarricoats, L. Shafai, and A. A. Kishk, *Microwave Horns and Feeds*, ser. IEE electromagnetic waves series, P. J. B. Clarricoats, Ed. London, United Kingdom: IEE, 1994, vol. 39.

[45] A. K. Bhattacharyya and G. Goyette, "A novel horn radiator with high aperture efficiency and low cross-polarization and applications in arrays and multibeam reflector antennas," *IEEE Trans. Antennas Propag.*, vol. 52, no. 11, pp. 2850–2859, 2004.

[46] X. Cheng, Y. Yao, J. Hirokawa, T. Tomura, T. Yu, J. Yu, and X. Chen, "Analysis and Design of a Wideband Endfire Circularly Polarized Septum Antenna," *IEEE Trans. Antennas Propag.*, vol. 66, no. 11, pp. 5783–5793, 2018.

[47] C. A. Balanis, *Antenna Theory: Analysis and Design*, 4th ed. Hoboken, New Jersey: John Wiley & Sons, Inc., 2016.

[48] T. S. Bird and C. Granet, "Optimization of Profiles of Rectangular Horns for High Efficiency," *IEEE Trans. Antennas Propag.*, vol. 55, no. 9, pp. 2480–2488, 2007.

[49] D. Dousset, S. Claude, and K. Wu, "A Compact High-Performance Orthomode Transducer for the Atacama Large Millimeter Array (ALMA) Band 1 (31–45 GHz)," *IEEE Access*, vol. 1, pp. 480–487, 2013.

[50] A. Navarrini and R. Nesti, "Symmetric Reverse-Coupling Waveguide Orthomode Transducer for the 3-mm Band," *IEEE Trans. Microw. Theory Techn.*, vol. 57, no. 1, pp. 80–88, 2009.

[51] T. J. Reck and G. Chattopadhyay, "A 600 GHz Asymmetrical Orthogonal Mode Transducer," *IEEE Microw. Wireless Compon. Lett.*, vol. 23, no. 11, pp. 569–571, 2013.

[52] C. A. Leal-Sevillano, K. B. Cooper, E. Decrossas, R. J. Dengler, J. A. Ruiz-Cruz, J. R. Montejo-Garai, G. Chattopadhyay, and J. M. Rebollar, "Compact Duplexing for a 680-GHz Radar Using a Waveguide Orthomode Transducer," *IEEE Trans. Microw. Theory Techn.*, vol. 62, no. 11, pp. 2833–2842, 2014.

[53] C. A. Balanis, "Polarization Measurements," in *Antenna Theory: Analysis and Design, 4th Edition*. Hoboken, New Jersey: John Wiley & Sons, 2016, ch. 17, p. 1017.

[54] T. King, S. Butcher, and L. Zalewski, "Apocrita - High Performance Computing Cluster for Queen Mary University of London," 3 2017. [Online]. Available: https://zenodo.org/record/438045

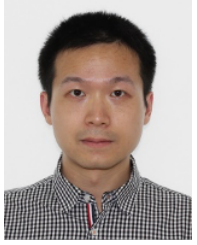

Chao Shu received the B.S. and M.S. degrees in communication and information system from Beijing University of Posts and Telecommunication, Beijing, China, in 2005 and 2008, respectively. From 2008 to 2016, he was with Datang Mobile Communications Equipment Co., Ltd, as a software engineer and then a division manager. He has joined Queen Mary University of London since 2016 and is currently working toward the Ph.D. degree.

His research interests include wideband circularly polarized antennas, millimeter wave and THz communication and imaging systems. He has authored a number of papers on these topics, and he holds 12 granted and pending China patents. He is a reviewer of several journals like IEEE Antennas and Wireless Propagation Letters, Physical Communication.

Shaoqing Hu received the B.S and M.S degrees in electronic engineering from the University of Electronic Science and Technology of China, Chengdu, Sichuan, China, in 2013 and 2016, and the Ph.D. degree in electronic engineering from Queen Mary University of London, London, UK, in 2020.

From 2020, he is a teaching fellow with the School of Electronic Engineering and Computer Science, Queen Mary University of London. He is the author of more than 10 articles. His research interests include antennas, arrays, millimeter wave and THz imaging.

Dr. Hu was a recipient of IEEE Asia-Pacific Conference on Antennas and Propagation Student Paper Award in 2015, and UK-Europe-China Workshop on Millimeter Waves and THz Technologies Best Student Paper Award in 2020. He is a reviewer of many journals like IEEE Access, IET Microwaves, Antennas & Propagation, International Journal of RF and Microwave Computer-Aided Engineering.

Xiaohe Cheng (S'17) received the B.Sc. degree from Hebei University, Baoding, China, in 2014. He is currently pursuing the Ph.D. degree in electronics and communication engineering from the Beijing University of Posts and Telecommunications, Beijing, China. Since 2017, he has been a Junior Visiting Fellow with the Ando and Hirokawa Laboratory, Tokyo Institute of Technology, Tokyo, Japan.

His current research interests include wideband antennas, circularly polarized antenna, high-gain millimeter-wave antennas.

Andre Sarker Andy (M'14) received the M.Sc. degree in mobile and wireless networks and the PhD degree in electronic engineering from Queen Mary University of London, UK, in 2013 and 2018 respectively. He is currently employed as a Technical Officer on an EPSRC project (TERRA) in Queen Mary University of London, UK.

From 2018 to 2019, he was a Postdoctoral Research Assistant for an ERC project (TERALINKS) involving terahertz high power links using photonic devices, tube amplifiers and beam-steerable antennas in Queen Mary. During his PhD he was also a Research Assistant for 6 months for another EPSRC project (Active Quasi-Optics for High-Power THz Science) in conjunction with RAL Space. His research interests include terahertz beam-forming, additive manufacturing for millimeter-wave and terahertz antennas, non-linear quasi-optical devices, metamaterials, photosensitive polymers and semiconductors, and antenna measurement systems.

Yuan Yao (M'11-SM'15) received the B.Sc. degree in Communication Engineering from Tianjin University, China, in 2004 and the Ph.D degree in Electronic Science and Technology from Tsinghua University, China, in 2010.

In April 2010, he joined the School of Electronic Engineering, Beijing University of Posts and Telecommunications. He is currently a professor at this university. His research interests include in the fields of antennas, RFID, and THz technology. He has published over 200 papers and three books.

Prof. Yao is currently an editor of *IEEE Access* and *International Journal of Antennas and Propagation*.

Bo Zhang (M'07-SM'15) received the B.E., M.S., and Ph.D. degrees in electromagnetic field and microwave technology from the University of Electronic Science and Technology of China, Chengdu, China, in 2004, 2007, and 2011, respectively.

He is currently a Professor with the School of Electronic Science and Engineering, University of Electronic Science and Technology of China. His research interest includes terahertz solid state technology and systems.

Yasir Alfadhl (M'09) received the B.S. degree in telecommunication engineering from the Queen Mary University of London, London, U.K., in 2000, and the Ph.D. degree in electromagnetics and antennas in telecommunication engineering from the University of London, London, in 2006. He started a post-doctoral project, where he designed and prototyped a novel base-station antenna for Semi-Smart cellular networks, as part of a consultancy project for the Office of Communication–regulatory authority body for the U.K. communications industries. He was a Knowledge Transfer Associate and the Manger in the industry, where he developed 3-D modeling methods for radar and telecom applications. Since 2009, he has served as a Faculty Member with the School of Electronic Engineering and Computer Science, Queen Mary University of London, as a joint-Program Lecturer. Since 2006, he has authored or co-authored over 30 publications. His current research interests include computational electromagnetics, high-power microwave devices, bio-electromagnetics, and dielectric properties of materials. Dr. Alfadhl was a member of the Organizing Committee in the IEEE International Workshop on Antenna Technology: Small and Smart Antennas Conference in Cambridge in 2007. He was nominated (one of the top 20 in the U.K.) by the Institute of Directors for the KTP Business Leader of Tomorrow Awards in 2009.

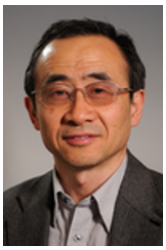

Xiaodong Chen (M'96–SM'07–F'14) received the B.Sc. degree in electronics engineering from the University of Zhejiang, Hangzhou, China, in 1983, and the Ph.D. degree in microwave electronics from the University of Electronic Science and Technology of China, Chengdu, China, in 1988.

He joined the Department of Electronic Engineering, King's College, University of London, London, U.K., in 1988, as a Postdoctoral Visiting Fellow. In 1990, he was employed by the King's College as a Research Associate and was appointed to a lectureship later on. In 1999, he joined the School of Electronic Engineering and Computer Science, Queen Mary University of London, London, where he is currently a Professor of Microwave Engineering with the School of Electronic Engineering and Computer Science. He is also the Director of the BUPT-QMUL Joint Research Lab, Beijing. He holds a Visiting Professorship with the University of Westminster, U.K., the Beijing University of Posts and Telecommunications (BUPT), and the University of Electronic Science and Technology of China. He has authored or coauthored over 400 publications (book chapters, journal articles, and refereed conference presentations). His current research interests include high-power microwave devices, wireless communications, and antennas.

Prof. Chen is a member of the U.K. Engineering and Physical Sciences Research Council Review College and the Technical Panel of the Institution of Engineering and Technology Antennas and Propagation Professional Network. He is a Fellow of IET/IEEE.